5-2016

The Effects of Rotation and River Discharge on Net Mixing in Small-Mouth Kelvin Plumes

Kelly Cole
University of Maine

Robert D. Hetland

The Effects of Rotation and River Discharge on Net Mixing in Small-Mouth Kelvin Number Plumes

KELLY L. COLE* AND ROBERT D. HETLAND

Department of Oceanography, Texas A&M University, College Station, Texas

ABSTRACT

Small-mouth Kelvin number plumes, or plumes with a source width smaller than the deformation radius, are characterized by near-field plume regions of rapid lateral expansion and strong vertical mixing. Net plume mixing, or the dilution of a plume by ocean water between the estuary mouth and the far-field plume, is examined using idealized numerical experiments with the Regional Ocean Modeling System (ROMS). The density anomaly of plume water entering the far field is determined from isohaline analysis of the modeled salinity field. The experiments indicate that when estuarine discharge increases, net plume mixing decreases in a rotating environment but increases in a nonrotating environment. Scaling analysis supports that this opposite trend in behavior is related to rotation turning the plume, limiting the lateral expansion and suppressing shear mixing. The results of this study explain different trends in net plume mixing reported in previous studies and compare favorably to observations of the Fraser River plume.

1. Introduction

Mixing in the region just seaward of a narrow estuarine discharge can significantly alter the water properties of a parcel, such that the water that eventually enters a geostrophic alongshore coastal current is substantially different from the water that left the estuary mouth. Much of this mixing happens very close to the source in the near-field river plume. The near-field plume is a region of rapid plume expansion and strong shear mixing (Chen and MacDonald 2006; MacDonald et al. 2007; Hetland and MacDonald 2008; McCabe et al. 2008). The strong mixing decays as a parcel is moved away from the source and transitions to the far field, where plume water becomes part of the larger-scale shelf circulation. This paper focuses on how estuarine discharge is transformed before it enters the far-field plume, which defines the water properties of the subsequent coastal current. Many models of far-field buoyancy-driven flow use source parameters, such as the density anomaly and discharge rate, to predict properties of the offshore shelf circulation (e.g., Garvine 1987; Yankovsky and Chapman 1997; Lentz and Helfrich 2002), so understanding how plume dilution through the near-field changes in response to inflow variables is essential.

The goal of this study is to understand how plume dilution between the source and far field varies with estuarine discharge and rotation in small-mouth Kelvin number plumes. The mouth Kelvin number $K = W/R_d$, where W is the source width and R_d is the baroclinic deformation radius, indicates plume behavior offshore. In this study, the source scale is smaller than the deformation radius (i.e., $K \leq 1$); the outflow is essentially uniform across the channel and radially spreading in the near field. Recent observational (Halverson and Pawlowicz 2008) and modeling (Hetland 2010) studies of small-mouth Kelvin number plumes indicate different trends in plume dilution, and this study reconciles their results. Halverson and Pawlowicz (2008) show that the Fraser River plume density anomaly increases with discharge in the Strait of Georgia, British Columbia, Canada from several years of ferry data. Hetland (2010) reports the opposite trend in plume dilution using an idealized near-field layer model. There are several differences in the experimental approach between the Halverson and Pawlowicz (2008) and Hetland (2010) studies; one

---

* Current affiliation: Darling Marine Center, University of Maine, Walpole, Maine.

Corresponding author address: Kelly L. Cole, Darling Marine Center, University of Maine, 193 Clarks Cove Rd., Walpole, ME 04573.
E-mail: kelly.cole@maine.edu

being that rotation is not incorporated into the layer model formulation, while the field measurements describe observations of a midlatitude geophysical-scale plume influenced by rotation.

Although observational and modeling studies show that rotation is an important factor in the plume momentum balance even within a kilometer of the estuary mouth (Chen et al. 2009; McCabe et al. 2009), it is often overlooked in studies of near-field mixing driven by advection and buoyancy. Rotation forces a midfield region—a transition between the near and far fields—where spreading is inhibited as the plume turns toward the coast, curtailing the enhanced mixing that spreading causes and thereby impacting plume dilution estimates offshore greatly. In this paper, the role of rotation in inhibiting near-field mixing is examined as the most likely cause for the disagreement between previous studies. Both Halverson and Pawlowicz (2008) and Hetland (2010) show that the near-field region grows proportionally to river discharge, suggesting an increased transit time of flow in the near field. However, geostrophic adjustment occurs at time scales of f^{-1}—independent of discharge—turning the flow anticyclonically and inhibiting plume spreading by trapping the plume to the coast (Kakoulaki 2015). Rotation will therefore limit the area over which plume spreading and enhanced shear mixing takes place.

2. Background

a. Plume regions

Spreading causes the pycnocline to shoal and the sea surface to drop. This drop in pressure corresponds to a decrease in the potential energy of the plume, which in turn causes an associated increase in the kinetic energy and an acceleration of the plume, as described by the Bernoulli relation. The accelerating plume increases the shear at the base of the plume, thereby enhancing shear instabilities and mixing within the plume (Hetland 2010). Generally, the strength of mixing decreases offshore and the separation between isohaline outcroppings increases. Eventually, in the absence of other forces, as the near-field plume returns to subcritical flow and local mixing rates decrease, the density anomaly associated with the near-field plume asymptotically approaches its far-field value. The mechanics of near-field mixing and spreading are captured in the plume lateral momentum balance, driven primarily by lateral pressure (density) gradients due to the interface slope, advection, and interfacial stress at the plume base. In a geophysical-scale plume, rotation begins to affect the flow as the plume scales with the deformation radius. Momentum shifts toward thermal wind balance; the lateral pressure gradients then drive along-stream flow instead of lateral spreading.

Garvine (1999) clearly illustrates how rotation limits plume spreading. We hypothesize that rotation decreases net mixing, as it effectively arrests the near field by redirecting streamlines to curve along the plume front.

Local mixing in the near field has been studied by Chen and MacDonald (2006), MacDonald et al. (2007), and McCabe et al. (2008) and the dilution of estuarine water through plumes is evaluated in several works of Garvine (1982, 1984, 1987), but it is difficult to synthesize dilution estimates from previous studies because dynamic plume regions (i.e., the near and far fields) are not consistently defined, if at all. Traditional definitions of plume regions are complicated by bathymetry and coastlines, tidal pulsing, ambient currents and wind, and it is unclear how influential these variables are throughout the plume. The near and far fields are typically defined as supercritical and subcritical plume regions, respectively. However, the decay of plume properties away from the source and gradual transition to the far field suggests that the near field should perhaps not be described as a discrete region (see Hetland 2010). Plume circulations indicate that there is often a transition region between the advection-driven near field and the geostrophic, Ekman-dominated far field—the midfield plume—where shear mixing wanes as spreading slows and offshore forcings can influence propagation. Through the near field and midfield, rotation may inhibit plume spreading, and consequently shear mixing, prior to the plume reaching its nonrotational far-field asymptotic density.

b. Geophysical-scale numerical studies

Idealized models configured with rectangular, narrow-mouth estuaries and straight coasts, similar to the model domain used in this study, have been applied in several investigations of buoyancy-driven shelf circulation (Garvine 1982, 1984, 1987; O'Donnell 1990; Yankovsky and Chapman 1997; Fong and Geyer 2001; Hetland 2005; Jurisa and Chant 2013). Seminal plume studies use reduced-gravity models to examine the effect of varying inflow properties on plume evolution offshore, describing the near-field plume structure particularly well (Garvine 1982, 1984, 1987; O'Donnell 1990). These studies show how parameters at the inflow affect the plume density anomaly and layer depth to influence expansion, but the plume dilution in different regions is not reported. An inviscid plume interior is assumed in the Garvine model series, with mixing occurring only at the frontal boundary; the front sets the plume interior depth and density structure as it travels offshore in the simulations (Garvine 1987; O'Donnell 1990). Plume interior mixing is parameterized in the more realistic layer model developed by O'Donnell (1990), but the

semicircular source application that prevents the plume from separating from the coast is a different approach to the problem than the study presented here.

Realistic plume evolution is achieved in studies using fully 3D hydrodynamic models. Yankovsky and Chapman (1997) build on previous layer model results through the use of a fully 3D idealized model coupled with steady, inviscid theory to describe the distance a plume spreads offshore. Plume dynamics are not explicitly divided into regions in Yankovsky and Chapman (1997), so the dilution of estuarine water through the near field is difficult to extract. Yankovsky et al. (2001) have investigated the impact of tidal and subinertial variations in discharge on plume structure using both pulsed harmonic forcing and single pulsed discharge events. Although the details of plume mixing are not evaluated, they conclude that subinertial variability in estuarine discharge greatly affects bulge dynamics and downstream circulation through the generation of the density field. Garvine (1999) examines how far a gravity current will travel along and cross shore with the fundamental parameters of the inflow before it is mixed away. This paper builds on that work by investigating the mixing between the river mouth and far-field plume and reveals similar key dimensionless inflow parameters.

c. Engineering-scale numerical studies

Engineering-scale modeling studies with idealized domains (Jirka 2007; Jones et al. 2007) describe the offshore extent and dilution of a plume in response to changes in transport, buoyancy, and momentum fluxes at the mouth, with descriptions of lateral and vertical structure and measures such as jet-to-plume and plume-to-cross-shore length scales, which are comparable to the near and far fields in geophysical-scale studies. However, engineering studies use a different source aspect ratio and often ignore rotation, which is a key topic in this paper. Furthermore, this study uses salinity coordinates to identify plume regions instead of length scales in Cartesian space, which is a more integrated way of looking at the plume because it allows for bulge asymmetry (MacCready et al. 2002; Hetland 2005).

3. Model

Numerical simulations are implemented using the Regional Ocean Modeling System (ROMS, version 3.5; Shchepetkin and McWilliams 2005), configured with a rectangular grid that represents a simplified estuary/shelf plume system. ROMS is a hydrostatic, free-surface, primitive equation model that is commonly used in coastal studies of buoyancy-driven flow. The domain is idealized but supports plume dynamics similar to the Merrimack River (Hetland and MacDonald 2008), Columbia River (McCabe et al. 2009), and Fraser River discharges. The dimensions of the domain are based on the Merrimack River estuary and plume, with a narrow mouth separating a wider estuary from the shelf; however, all plumes with a narrow source will spread and mix in the near field similarly. Figure 1 shows the model domain. The grid is 35 km long in the cross-shore direction and 71.2 km long in the alongshore direction with a horizontal grid spacing of 100 m in both directions and open boundaries upcoast, downcoast, and offshore. The river discharge is specified at the western edge, at the upstream end of the estuary.

The simulations use 20 irregularly spaced vertical layers stretched at the free surface and the bottom, with $\theta_s = 3.0$, $\theta_b = 0.25$, and $h_c = 5$ m, giving nearly 0.5-m vertical resolution of the plume. In the medium discharge experiments, this typically provides at least seven grid cell resolution of the plume layer and even finer resolution near the estuary mouth. Bottom topography is flat at 15-m depth over the shelf and sloping in the estuary with a minimum 5-m depth at the head and maximum 15-m depth at the mouth in the vertical. The estuary is rectangular with a contraction at the mouth 500 m wide and 1 km long; the total length of the estuary is 8.5 km. Rotating experiments are performed on an f plane at 6°N ($f = 1.52 \times 10^{-5}\,\text{s}^{-1}$), 22°N ($f = 5.45 \times 10^{-5}\,\text{s}^{-1}$), 45°N ($f = 1.0 \times 10^{-4}\,\text{s}^{-1}$), and 70°N ($f = 1.37 \times 10^{-4}\,\text{s}^{-1}$). The Congo, Pearl, Merrimack, and Colville River mouths are at these approximate latitudes.

The plume develops through riverine buoyancy forcing, with an ambient salinity of $32\,\text{g}\,\text{kg}^{-1}$ initialized in the oceanic portion of the domain and freshwater of $0\,\text{g}\,\text{kg}^{-1}$ entering the domain at the head of the estuary. A semidiurnal tide is incorporated into the model by raising and lowering the free surface at the open boundaries as a sine wave with a 12-h period; the tidal phase is referenced to the sea surface height at the estuary mouth in the following analyses. A $5\,\text{cm}\,\text{s}^{-1}$ southward-flowing barotropic coastal current that spans the oceanic portion of the domain is forced at the northern open boundary. Flather and Chapman conditions are applied at the open boundaries for the barotropic velocity components and free surface, respectively, which allows fluid flow out of the domain (Flather 1976; Chapman 1985). Three-dimensional velocity components and tracers follow a radiation open boundary condition (Marchesiello et al. 2001). The model is initialized to oceanic salinity, a flat sea surface and a $5\,\text{cm}\,\text{s}^{-1}$ downcoast flow.

Vertical mixing is described by the k–ϵ turbulence closure coupled with Canuto A stability function formulation (Canuto et al. 2001). Quadratic bottom friction is incorporated into the momentum equation and conservative, parabolic spline reconstruction is used for
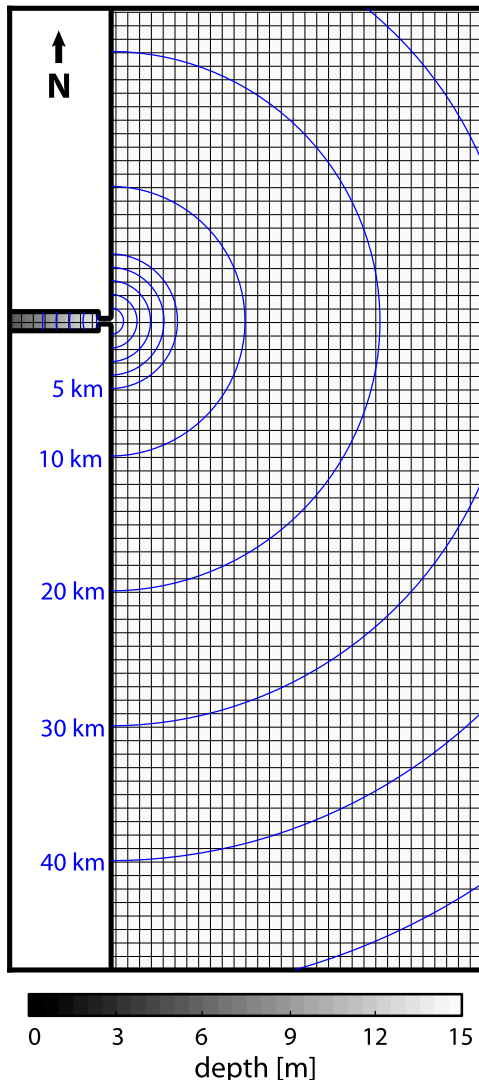
FIG. 1. Model grid and bathymetry. Black lines mark every 10 grid spaces. Blue lines are radial distances from the mouth in kilometers (1, 2, 3, 4, 5, 10, 20, 30, 40, and 50 km shown). Gray filled contours indicate water depth. The shallowest point at the head of the estuary is 5 m, and the shelf depth is 15 m.

vertical derivatives in the model. A background horizontal Laplacian diffusion of tracers with a coefficient of $1 \, \text{m}^2 \, \text{s}^{-1}$ is used to damp numerical instabilities, with horizontal mixing of tracers along geopotential surfaces. Horizontal and vertical tracer advections are calculated using the multidimensional positive definite advection transport algorithm (MPDATA; Smolarkiewicz and Clark 1986).

Each simulation is run for approximately one week. Model simulations are evaluated over two averaged tidal cycles on the fifth day of the simulation. Plume mixing and entrainment is an inherently tidal process, but the numerical results suggest that there is negligible change in plume structure over a tide, so subtidal fields are analyzed. Discharge rates of $Q_f = 100, 250, 500, 1000, 1800$, and $2800 \, \text{m}^3 \, \text{s}^{-1}$ are implemented in the model paired with a 1.5-m tide. Figure 2 illustrates low and high discharge $f = 10^{-4} \, \text{s}^{-1}$ scenarios over a tidal cycle. The parameter space consists of 21 model simulations: $Q_f = 100, 250, 500, 1000, 1800$, and $2800 \, \text{m}^3 \, \text{s}^{-1}$ discharges are completed with $f = 10^{-4} \, \text{s}^{-1}$ and without rotation, and discharge scenarios of $Q_f = 100, 1000$, and $2800 \, \text{m}^3 \, \text{s}^{-1}$ are completed with $f = 1.52 \times 10^{-5}, 5.45 \times 10^{-5}$, and $1.37 \times 10^{-4} \, \text{s}^{-1}$.

Table 1 shows tidal mean inflow parameters for the rotational experiments with $f = 10^{-4} \, \text{s}^{-1}$. The value $R_d = \sqrt{g'h}/f$ is the baroclinic Rossby radius of the inflow, where f is the Coriolis frequency, $g' = g\Delta\rho/\rho_0$ and h are reduced gravity and depth at the estuary mouth, g is gravity, $\Delta\rho$ is the inflow density anomaly, and ρ_0 is the ambient density. The value $\text{Ro} = U/fW$ is the mouth Rossby number, where U is the mean velocity of the inflow, and W is the mouth width. The estuary mouth width is kept constant in these numerical experiments. The value $S = R_d/W$ is the Burger number of the inflow, and $\text{Fr} = \text{Ro}/S = U/\sqrt{g'h}$ is the inflow Froude number. The large values for Ro and S indicate that rotation has little effect near the source; the small-mouth width significantly constricts the flow, creating a strong jetlike discharge. However, the buoyancy of the inflow influences plume evolution more than advection, given the subcritical inflow Froude numbers; this is evidenced by the surface-advected plumes shown in Fig. 2 (Yankovsky and Chapman 1997).

The density of the inflow into the shelf portion of the domain is set by estuarine dynamics. Plume structure is altered in the different discharge cases by the amount of ocean water able to enter the estuary and be subsequently mixed into the upper layer that feeds the plume. Interfacial mixing is the primary mixing mechanism in the estuary. The bottom is sloping, and in the low discharge case the fresh upper layer lifts off at the head and has little interaction with the bottom; the estuary is vertically stratified and does not exhibit a partially mixed state. As discharge increases, the estuary shortens and a time-dependent salt wedge forms that changes position within the estuary over the tide. Isohalines interact with the bottom in this case, and bottom stress impacts estuarine mixing. Additionally, when discharge is low, a tidal intrusion front brings plume water into the estuary full water column during flood, and bottom mixing is likely important at this time near the mouth.

4. Methods

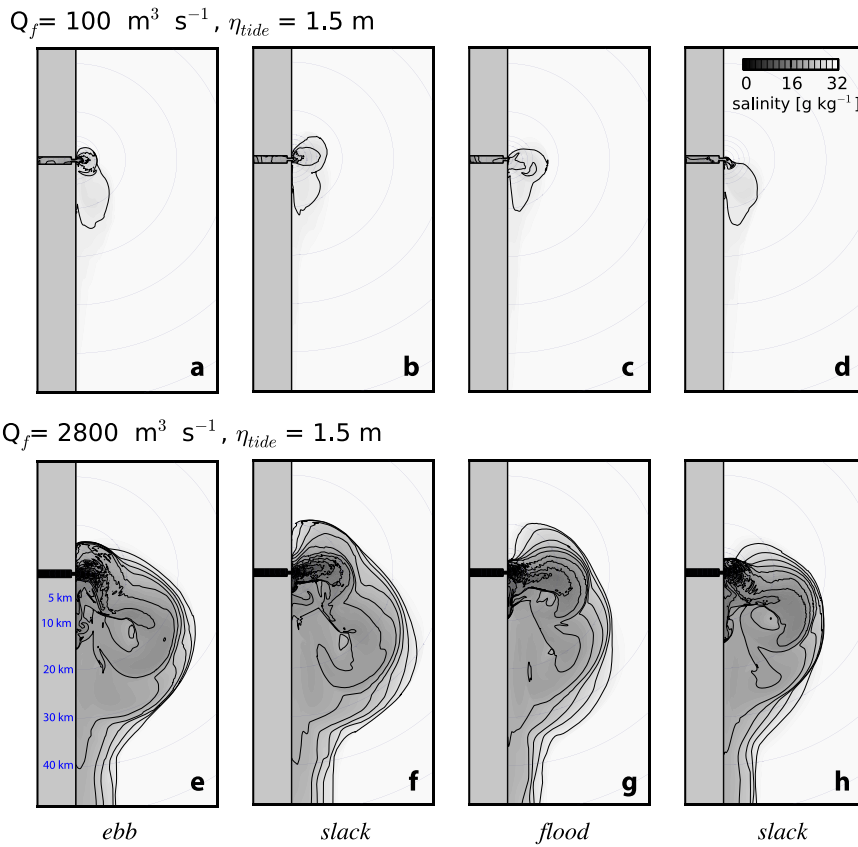The schematic in Fig. 3 illustrates a vertical section through the core of the plume at late ebb, with an axially

Q_f= 100 m^3 s^{-1}, η_{tide} = 1.5 m

Q_f= 2800 m^3 s^{-1}, η_{tide} = 1.5 m

ebb   *slack*   *flood*   *slack*

FIG. 2. Time sequence of surface salinity for the (top) $Q_f = 100\,\mathrm{m^3\,s^{-1}}$ and (bottom) $Q_f = 2800\,\mathrm{m^3\,s^{-1}}$ with $f = 10^{-4}\,\mathrm{s^{-1}}$ cases. (a),(e) Surface salinity at max ebb; (b),(f) surface salinity at low water; (c),(g) surface salinity at max flood; and (d),(h) surface salinity at high water. Phases of the tide are labeled with respect to the sea surface elevation at the center grid cell at the estuary mouth. Blue lines are radial distances from the mouth.

varying, slablike plume salinity structure and a thin pycnocline, similar to that discussed in Hetland (2005). Although the experiments presented here are tidally forced, much physical insight can be gained from a steady-state layer formulation. In a steady state, the vertical mixing within the plume may be related to the surface area of different salinity classes within the plume, a relationship given by

$$w_e(s_0 - s_A)\frac{\partial A}{\partial s_A} \sim Q_f, \qquad (1)$$

where $w_e(s_0 - s_A)$ is the average vertical salt flux associated with the surface salinity range s_A, s_0 is the background salinity, w_e is the vertical entrainment velocity, A is the surface area of salinity range s_A, and Q_f is the river discharge. Thus, the regions of rapid change in surface salinity are associated with high mixing. Because the plume thickness remains relatively constant compared to changes in its horizontal extent, a similar relationship holds for the volume of different salinity classes. A large

volume of water at a particular salinity indicates waters associated with weak mixing. This relation provides the physical basis for the isohaline definition of plume regions in this study. We define the near-, mid-, and far fields as mixing regions in isohaline space. Isohaline freshwater volume and vertical turbulent buoyancy flux are used to identify plume regions qualitatively by

TABLE 1. Tidal mean dimensional and nondimensional parameters at the inflow for experiments with $f = 10^{-4}\,\mathrm{s^{-1}}$. Columns show river discharge, the baroclinic deformation radius R_d, the Rossby number Ro, the Burger number S, and the Froude number Fr.

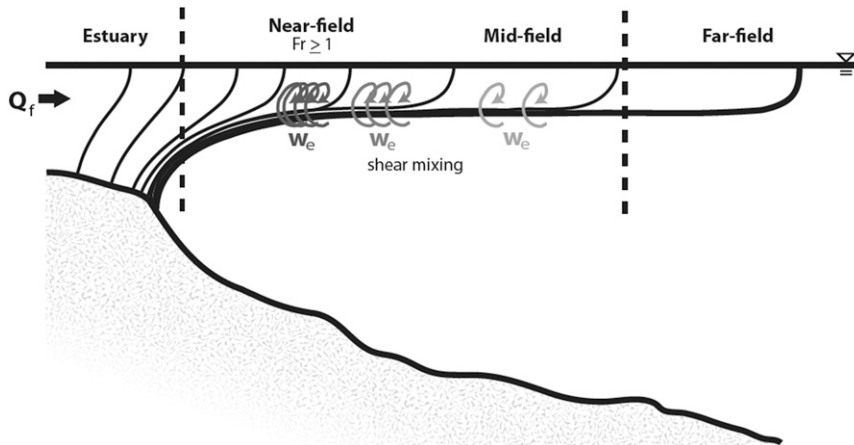| Discharge $(\mathrm{m^3\,s^{-1}})$	R_d (km)	Ro	S	Fr
100	11.08	7.66	22.17	0.35
250	14.57	10.79	29.15	0.37
500	17.10	14.30	34.20	0.42
1000	18.81	18.67	37.63	0.50
1800	19.08	22.99	38.15	0.60
2800	19.09	26.59	38.18	0.70

FIG. 3. Schematic illustrating plume isohaline vertical structure. Thin, black lines are isohalines. The term Q_f indicates the freshwater inflow. Dark gray, curled arrows represent strong entrainment, and light gray, curled arrows represent weak entrainment. Dotted lines mark the separation between the estuary, near-field, and far-field plumes.

assessing mixing strength in an isohaline relative to other plume isohalines. The near field is the region with relatively low isohaline freshwater volume at low salinity classes, indicating strong mixing. The midfield is the region with rapid, increasing change in isohaline freshwater volume with increasing salinity, indicating diminished mixing toward ocean isohalines. The discrete division between the near field and midfield is where the Froude number becomes subcritical; however, mixing diminishes and isohalines expand offshore in both regions. The far field is the region with relatively high isohaline freshwater volume, indicating weak mixing. The transition isohaline between the near/midfield to the far-field plume defined by isohaline freshwater volume in salinity space is critical to our estimation of plume dilution.

Plume dilution is termed "net" mixing in this study. The net mixing that a water parcel experiences as it transitions through the near-field and midfield plumes, a measure of the total dilution of a parcel of plume water by ocean water before it enters the far field, is proportional to, but distinct from, the "local" mixing. The net mixing depends on the mixing history of a water parcel and the length of time that parcel stays within the near-field plume. Net mixing is defined as the change in plume density anomaly between the estuary mouth and the point where local mixing has diminished, where a water parcel enters the coastal current or far-field plume.

The ratio of the density anomaly offshore to the density anomaly at the estuary mouth $\Delta\rho_{\text{bulge}}/\Delta\rho_i$ is evaluated to estimate trends in net plume mixing. We define $\Delta\rho_i = \rho_0 - \rho_i$ and $\Delta\rho_{\text{bulge}} = \rho_0 - \rho_{\text{bulge}}$, where ρ_0 is the ambient density; ρ_i is the tidally averaged, transport-weighted mean

density of outflowing water at the estuary mouth; and ρ_{bulge} is the density of water entering the far field. Note that the bulge is a rotational phenomenon, and in the rotational experiments, $\Delta\rho_{\text{bulge}}$ is related to the density anomaly of water leaving the rotational bulge, but in nonrotational experiments $\Delta\rho_{\text{bulge}}$ simply represents the density anomaly of plume water entering the far field; they are labeled similarly for comparison.

The far-field density anomaly $\Delta\rho_{\text{bulge}}$ is the asymptotic limit of the plume density anomaly and is evaluated differently in rotational and nonrotational experiments. In nonrotational plumes, vertical mixing decays gradually offshore, making it difficult to identify plume mixing regions in isohaline space so another method is applied. Net mixing trends are comparable between the rotational and nonrotational cases, but because different methods are used to evaluate the far-field density anomaly, the exact values of $\Delta\rho_{\text{bulge}}/\Delta\rho_i$ are not comparable.

In nonrotating experiments, the density anomaly is calculated using the method described in Umlauf et al. (2007) and Hetland (2010). The first and second moments of the density anomaly $\Delta\rho$ are evaluated using

$$\Delta\rho h = \int_{-H}^{\eta} (\rho_0 - \rho)\,dz, \qquad (2)$$

and

$$\frac{1}{2}\Delta\rho h^2 = \int_{-H}^{\eta} (\rho_0 - \rho)z\,dz, \qquad (3)$$

where z is the vertical coordinate, and integration is from the sea surface η to the ocean bottom H. The background density ρ_0 is the density corresponding to

the ocean reference salinity ($s_0 = 32\,\mathrm{g\,kg^{-1}}$). Similar to the method described in Hetland (2010), an exponential decay function is fit to the inshore portion of the curve where the concavity is positive; the asymptotic limit of the density anomaly is the far-field density anomaly.

Coastal trapping of the plume by rotation results in a nonexponential shape of the density anomaly away from the river mouth, so a different method of evaluating $\Delta\rho_{\mathrm{bulge}}$ is used. In the rotational experiments, ρ_{bulge} is determined from the plume salinity class that displays the peak isohaline freshwater volume. Isohaline freshwater volume $\partial V_f / \partial s_A$ is evaluated from a volume integration of the freshwater fraction:

$$V_f(s_A) = \int_{s \leq s_A} \frac{s_0 - s}{s_0} dV. \tag{4}$$

An analogy can be made where the total freshwater contained within an isohaline V_f is similar to a cumulative probability distribution, and the isohaline freshwater volume $\partial V_f / \partial s_A$ is then similar to a probability distribution function. The term V_f gives the cumulative freshwater volume in an isohaline spanning many salinities, including the fresh endmember, while $\partial V_f / \partial s_A$ gives the freshwater content in the smaller range ∂s_A; $\partial V_f / \partial s_A$ is a "differential" freshwater volume, as termed in previous studies using isohaline coordinates (MacCready et al. 2002). The isohaline freshwater volume distribution can be interpreted as a histogram of freshwater content over the range of isohalines in the model domain. The surface of the isohaline s_A is the bound for integration, and $s_0 = 32\,\mathrm{g\,kg^{-1}}$ is the oceanic reference salinity.

A critical salinity for each experiment is identified where the maximum plume freshwater volume (or surface area) occurs in isohaline space, associated by Eq. (1) to a minimum in entrainment at that salinity class. This salinity class corresponds to water entering the far field. We evaluate ρ_{bulge} using this salinity class; low isohaline mean entrainment ($\leq 10^{-5}\,\mathrm{m\,s^{-1}}$) occurs at this salinity, consistent with entrainment values in a wind-free far field. Isohalines fresher than this salinity class exhibit approximate exponential growth of freshwater volume and diminishing mean entrainment toward higher salinities, characteristic of a slowing near field. The breakpoints in isohaline freshwater volume identify the far field and therefore dilution through the near- and midfield is incorporated into our net mixing estimate.

5. Results

a. Plume isohaline structure

Figure 4 shows an example of surface salinity from the $Q_f = 1000\,\mathrm{m^3\,s^{-1}}$ experiments with $f = 10^{-4}\,\mathrm{s^{-1}}$ and without rotation in Figs. 4a and 4b, respectively. The extent of the spreading plume region is significantly different between the two cases. In the $Q_f = 1000\,\mathrm{m^3\,s^{-1}}$ case, the distance from the mouth to the $32\,\mathrm{g\,kg^{-1}}$ contour in the offshore direction is ~15 km in the rotational case, while the $32\,\mathrm{g\,kg^{-1}}$ contour leaves the domain in the nonrotational case. The plume surface area is much larger in the nonrotational cases compared to the $f = 10^{-4}\,\mathrm{s^{-1}}$ cases. Clearly, the rotational and nonrotational simulations are fundamentally different in terms of density structure.

The vertical turbulent buoyancy flux B, defined by

$$B = -\frac{g}{\rho_0} K_\rho \frac{\partial \rho}{\partial z}, \tag{5}$$

where g is gravity, ρ density, ρ_0 is the reference density, K_ρ is the eddy diffusion coefficient, and z is the vertical coordinate, is averaged in isohalines to compare plume dilution between the river mouth and far-field plume. Chen and MacDonald (2006), MacDonald et al. (2007), and McCabe et al. (2008) report measures of near-field vertical turbulent buoyancy flux of $O(10^{-5})$ to $O(10^{-4})\,\mathrm{m^2\,s^{-3}}$. Strong local mixing of this magnitude is associated with isohaline-averaged mixing in this study of an order of magnitude smaller [$O(10^{-6})$ to $O(10^{-5})\,\mathrm{m^2\,s^{-3}}$]. The average is lower because the mixing in an isohaline diminishes away from the plume spreading axis.

Figure 5 shows isohaline-averaged vertical turbulent buoyancy flux for the $Q_f = 1000\,\mathrm{m^3\,s^{-1}}$ and $Q_f = 2800\,\mathrm{m^3\,s^{-1}}$ cases with $f = 10^{-4}\,\mathrm{s^{-1}}$ and with no rotation. The term B is calculated at each grid cell and binned by salinity, and the volume-weighted mean value is calculated for each salinity class. Isohalines of near-oceanic salinity interact with the boundary in nonrotational cases, so estimates of mean isohaline vertical turbulent buoyancy flux are contaminated by the boundary for salinities greater than $25\,\mathrm{g\,kg^{-1}}$ in the high discharge cases.

Local mixing at high salinity classes (around $20\,\mathrm{g\,kg^{-1}}$) is nearly an order of magnitude larger in the nonrotational cases than in the rotational cases. The drop-in vertical turbulent buoyancy flux at salinity classes near $20\,\mathrm{g\,kg^{-1}}$ in the rotational cases indicates the slowing of the near-field to subcritical velocities; the drop occurs at a lower salinity in the high discharge case. The transition to the far field happens gradually but at a higher salinity in the nonrotational, high discharge case. Thus, the salinity of water entering the far field is fresher at higher discharge in the rotational experiments and saltier in the nonrotational experiments, clearly showing that rotation inhibits the spreading near field before it is mixed to its nonrotational, far-field asymptotic value.

Figures 6a and 6c show surface salinity and a vertical section of salinity in the $Q_f = 500\,\mathrm{m^3\,s^{-1}}$ and $f = 10^{-4}\,\mathrm{s^{-1}}$

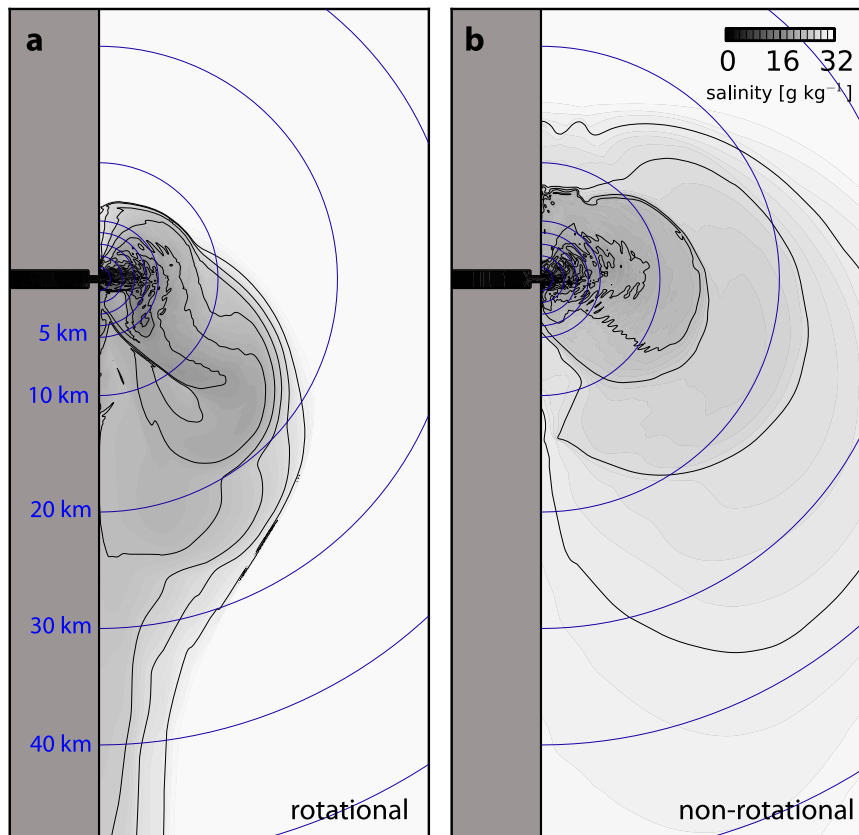$$Q_f = 1000 \ \text{m}^3 \ \text{s}^{-1}, \ \eta_{tide} = 1.5 \ \text{m}$$

FIG. 4. Surface salinity at late ebb for $Q_f = 1000 \, \text{m}^3 \, \text{s}^{-1}$ experiments (a) with $f = 10^{-4} \, \text{s}^{-1}$ and (b) without rotation. A $5 \, \text{cm} \, \text{s}^{-1}$ southward-flowing barotropic coastal current is forced at the northern boundary. Blue lines are radial distances from the mouth.

plume simulation during midebb. Figure 6b shows isohaline freshwater volume in the shelf portion of the domain. Salinity is divided into $1 \, \text{g} \, \text{kg}^{-1}$ bins, and the freshwater volume in each bin is determined from differentiating Eq. (4) with respect to salinity. The largest isohaline freshwater volume occurs at s_0, but this peak is removed in the figure to focus on plume isohalines. Note that freshwater volume has a similar structure across different phases of the tide, indicating that the plume is in roughly steady state even at time scales much smaller than the tidal time scale.

The vertical salinity structure in the plume along the transect shown in Fig. 6c is similar to the vertical structure illustrated in the schematic in Fig. 3, and the resultant isohaline freshwater volume distribution can similarly be decomposed into plume regions. The small freshwater volume in isohalines between 0 and $16 \, \text{g} \, \text{kg}^{-1}$ corresponds to the very near field of the plume. Here, water is quickly mixed to higher salinity classes. Freshwater pools in offshore isohalines greater than $\sim 16 \, \text{g} \, \text{kg}^{-1}$.

Freshwater volume is greater in these isohalines and increases toward higher salinity classes, indicating decreasing mixing. The slope of the curve up to $\sim 27 \, \text{g} \, \text{kg}^{-1}$ is a reflection of the expansion of plume isohalines offshore as mixing slows, consistent with the exponential decay of the plume density anomaly away from the source shown in previous studies (Hetland 2010). Freshwater near the source is rapidly mixed to the $27 \, \text{g} \, \text{kg}^{-1}$ isohaline; however, reduced local mixing at that salinity class requires a correspondingly larger surface area to mix freshwater to yet higher salinity classes. Marked by the transition from blues to grays in the colorbar in Fig. 6a, this salinity class represents the edge of the bulge region of the plume and is characteristic of water entering the coastal current or far field. The bounding isohaline used to define plume regions varies with Q_f; the plume dilution from the outflow salinity to $27 \, \text{g} \, \text{kg}^{-1}$ is used to estimate net mixing in the $Q_f = 500 \, \text{m}^3 \, \text{s}^{-1}$ with $f = 10^{-4} \, \text{s}^{-1}$ case shown in Fig. 6.
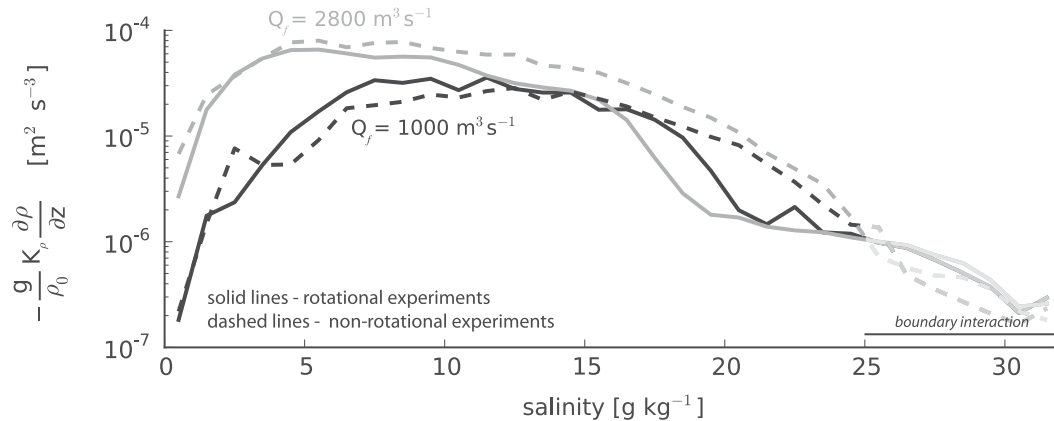
FIG. 5. Mean (over ebb) isohaline vertical turbulent buoyancy flux for the $Q_f = 1000\,\mathrm{m^3\,s^{-1}}$ (black lines) and $Q_f = 2800\,\mathrm{m^3\,s^{-1}}$ (gray lines) experiments with $f = 10^{-4}\,\mathrm{s^{-1}}$ (solid lines) and without rotation (dotted lines). The transparent region marks where isohalines interact with the offshore boundary in the nonrotational cases.

Figure 7 shows the tidal mean isohaline freshwater volume for several experiments varying Q_f with $f = 10^{-4}\,\mathrm{s^{-1}}$. The curves are colored by freshwater flushing times T_f defined by

$$T_f = \frac{V_f}{Q_f}, \qquad (6)$$

where V_f is the total freshwater contained within an isohaline given by Eq. (4). Isohalines with extremely small freshwater volume are not included in the calculation of flushing time; a cutoff proportional to the estuarine discharge over a tide and the inflow density anomaly is applied. The peak salinity of freshwater volume freshens as the discharge increases, indicating a fresher far field in each case. These isohalines flush freshwater on time scales close to the inertial period ($\sim$17.5 h for $f = 10^{-4}\,\mathrm{s^{-1}}$ simulations), further supporting the division between the near/midfield region and the far-field coastal current. This confirms that the time scales in the plume are quite small within the near field, such that the plume structure is in roughly steady state at any point in the tide.

The different density structures shown in Fig. 4 are reflected in the significantly different curves for the rotational and nonrotational $Q_f = 1000\,\mathrm{m^3\,s^{-1}}$ experiments shown in Fig. 7. The key difference is the local peak freshwater volume displayed in the rotational curve and the absence of the peak in the nonrotational curve, indicating a relatively large pool of freshwater in a coastally trapped isohaline in the rotational case. The freshwater retained in this isohaline is not mixed to higher salinity classes, as in the nonrotational case, because of the suppression of the shear-mixing region by rotation. Furthermore, relatively low isohaline freshwater

volume for the nonrotational $Q_f = 1000\,\mathrm{m^3\,s^{-1}}$ case at all salinities relative to the rotational case indicates that rotation influences the plume structure even near the source. Spreading and mixing is slowed significantly in the rotational near field.

b. The effect of rotation on net mixing

Figure 8 shows $\Delta\rho_{\mathrm{bulge}}/\Delta\rho_i$, the ratio of the far-field density anomaly to the density anomaly at the source, as a function of RoFr^{-2}, where Ro and Fr are inflow Rossby and Froude numbers in the rotational experiments. The density anomaly ratio is always less than one because of plume entrainment; the plume density offshore is greater than the plume density at the mouth, thus the density difference with respect to ambient water is smaller offshore. The Rossby and Froude numbers are calculated from the estuary mouth width, discharge-weighted mean outflow velocity at the estuary mouth, mean upper-layer depth of the outflow at the estuary mouth, and $\Delta\rho_i$. The Fr^{-2} term gives the collapse of data with the highest log-linear correlation.

As RoFr^{-2} increases, $\Delta\rho_{\mathrm{bulge}}/\Delta\rho_i$ tends to decrease, indicating an increase in net plume mixing. The $\mathrm{RoFr}^{-2} \simeq S\mathrm{Fr}^{-1}$, where S is an inflow Burger number that measures the importance of rotation at the estuary mouth: the larger the Burger number, the weaker the impact of rotation and more mixing in the plume, given the same Froude number.

For the same discharge, increasing rotation will decrease net mixing because the bulge shrinks with the deformation radius. The near-field grows with discharge, increasing the transit time of flow through the plume, but rotation inhibits spreading on a time scale independent of discharge, completely turning the plume downcoast
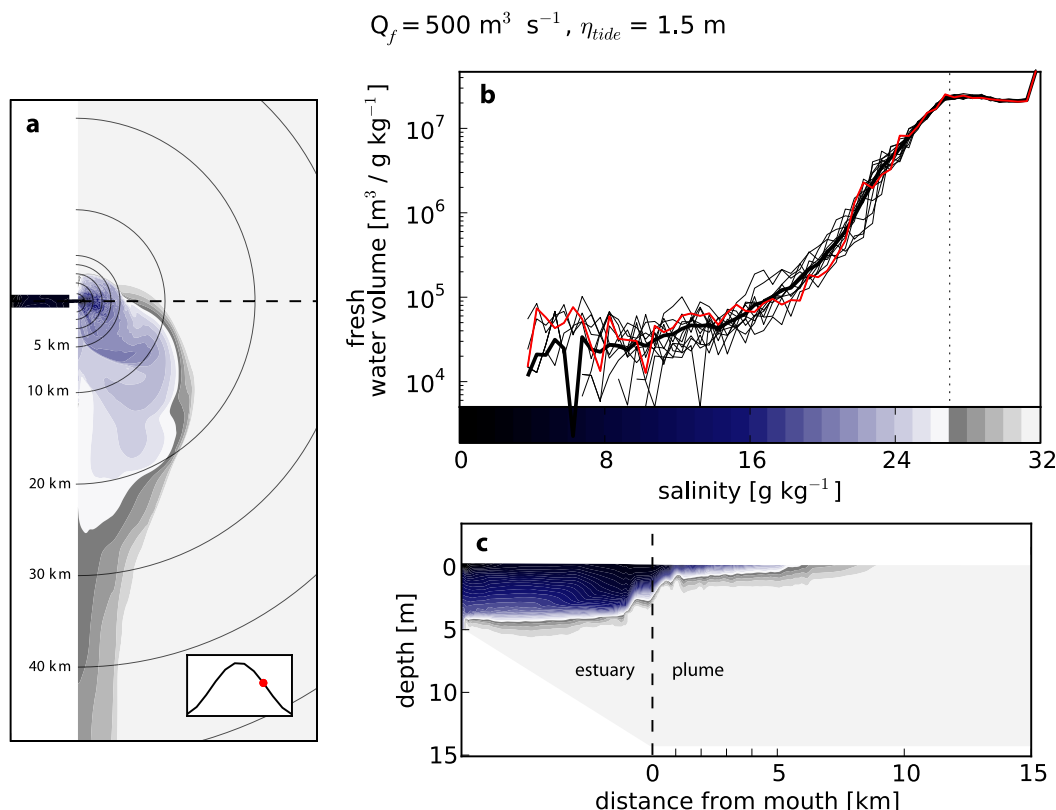
FIG. 6. (a) Surface salinity at midebb for the $Q_f = 500 \, \mathrm{m^3 \, s^{-1}}$ experiment with $f = 10^{-4} \, \mathrm{s^{-1}}$ (time is indicated by red dot on inset panel showing sea surface elevation over a tide). (b) Isohaline freshwater volumes. Thin, black lines represent isohaline freshwater volumes hourly during a tide, and the thick, black line shows the tidally averaged isohaline freshwater volumes. The red line marks freshwater volumes at midebb (same time as the other panels). The transition from blues to grays in the colorbar corresponds to the peak in freshwater volume that corresponds to the salinity of water entering the far field. (c) A cross section of salinity at midebb through the transect marked by the dashed line in panel (a). The colorbar in panel (b) applies to all panels.

before the plume salinity is mixed to its (nonrotational) far-field asymptotic value.

c. Net mixing in nonrotating plumes

Figure 9 shows the density anomaly in the shelf domain by radial distance from the mouth for the $Q_f = 500 \, \mathrm{m^3 \, s^{-1}}$ experiment without rotation. The tidal-mean density anomaly along an offshore transect from the estuary mouth exhibits an approximate exponential decay within the first 10 km of the mouth in the nonrotational case; the limit of an exponential decay function fit to these data represents the density anomaly of water entering the far-field plume.

Similar to Hetland (2010), $\Delta\rho_\mathrm{bulge}/\Delta\rho_i$ is shown as a function of $W_i^2 Q_f^{-1}$ in Fig. 10a, where Q_f and W_i are discharge and estuary mouth width for $f = 10^{-4} \, \mathrm{s^{-1}}$ and nonrotating simulations. The variability of the salinity components of the ratio are shown in Fig. 10b. We compare the simulated $\Delta\rho_\mathrm{bulge}/\Delta\rho_i$ to observations of the Fraser River plume presented in Halverson and Pawlowicz (2008).

Halverson and Pawlowicz (2008) show mean Fraser plume salinity and reference salinity as a function of the river discharge rate from ~4 yr of ferry data (Fig. 5 in Halverson and Pawlowicz 2008). Details of the data, including how the plume boundary is chosen, are explained in appendix B of Halverson and Pawlowicz (2008). We estimate the density anomaly from the salinity observations (used to calculate ρ_bulge and ρ_0). No information at the river mouth is available in Halverson and Pawlowicz (2008), so we compare the plume density anomaly to the freshwater density anomaly. This is reasonable since freshwater often reaches the mouth during moderate ebb discharges (MacDonald and Geyer 2004). At low discharge, $\Delta\rho_i$ could be smaller than the freshwater density anomaly (Kostaschuk and Atwood 1990), leading to larger values of the density anomaly ratio that could steepen the slope of the curve in Fig. 10a. It is the positive/negative character of the slopes of the curves in Fig. 10 that support our conclusion.

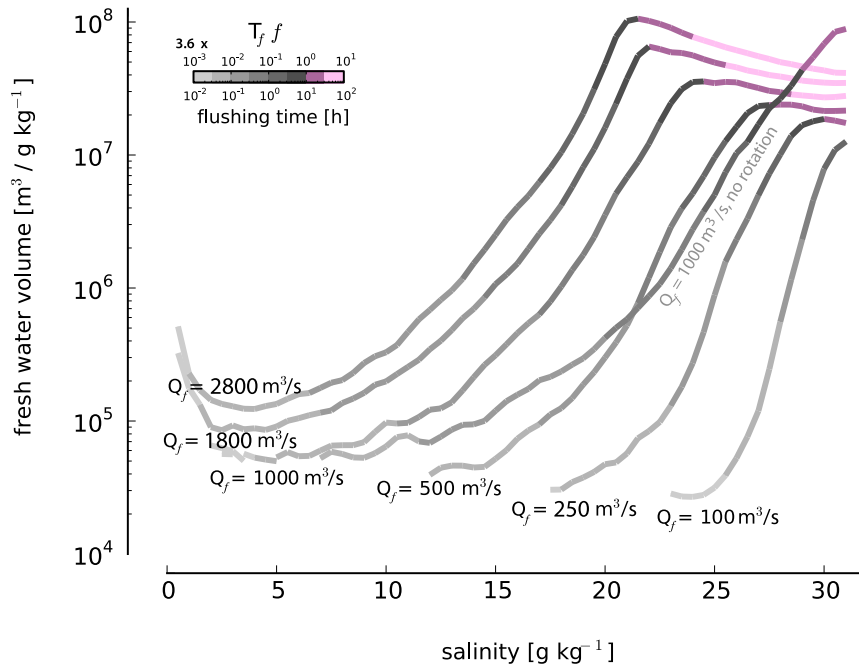We assume the width of the Fraser estuary mouth is ~1 km; there is a jetty to the north and tidal flats to the

FIG. 7. Tidal mean isohaline freshwater volumes for different discharge experiments with $f = 10^{-4}\,\text{s}^{-1}$. The $Q_f = 1000\,\text{m}^3\,\text{s}^{-1}$ case without rotation is also shown. Colors indicate flushing times of freshwater in isohalines (labeled on the bottom of the colorbar). The pink colormap indicates flushing times greater than the inertial period (far-field region). The top of the colorbar shows time scales normalized by the rotational parameter $f \sim 10^{-4}\,\text{s}^{-1}$. Regions where $T_f > f^{-1}$ correspond to salinity classes higher than the peak freshwater volume in each curve. The nondimensionalized flushing time ($T_f f$ scale above the colorbar) does not apply to the nonrotational case shown in the figure.

south of the mouth that extend ~1.5 km farther offshore than the jetty. Although the channel is narrow, the bathymetric break (defined by the 12-m isobath), and thus the salt front, follows a ~1-km diagonal across the mouth from the edge of the tidal flats to nearly the end of the jetty (MacDonald and Geyer 2005).

The observations and rotational model runs show a similar trend, implying that in a geophysical-scale plume, as river discharge increases, net mixing decreases. Without rotation, the spreading region is extensive and shear mixing occurs over a larger interfacial area, producing the opposite trend in net mixing. Note that $W_i^2 Q_f^{-1}$ has units of seconds per meter; the inverse velocity unit is related to an entrainment velocity, but it is difficult to extract a meaningful entrainment value representative of each experiment when a full closure is used. A dimensional comparison is reasonable in this case since the numerical experiments and the Fraser have similar geometry and discharge.

6. Discussion

Numerical experiments in this study address the net mixing response of a river plume to increasing freshwater discharge with varying rotational forcing. Our experiments produce results in agreement with both Halverson and Pawlowicz (2008) and Hetland (2010), thus explaining the discrepancy they present in the relationship between net mixing and freshwater discharge. As river discharge increases in the estuary plume system, the net mixing in a geophysical-scale plume influenced by rotation will decrease, and in a nonrotational plume the net mixing will increase. We explain this difference as an effect of rotation decelerating the plume and limiting the size of the near field where shear mixing occurs. The near-field area grows linearly with discharge in nonrotational experiments. Figure 4 indicates a fundamentally different horizontal density structure between rotational and nonrotational experiments, so different trends in net plume mixing are expected.

Figure 10a shows contrasting trends in $\Delta\rho_{\text{bulge}}/\Delta\rho_i$ between the rotational and nonrotational cases. Similar trends in $\Delta\rho_{\text{bulge}}/\Delta\rho_i$ are seen by inflow Froude, Rossby, and Burger numbers, as these parameters influence the size and position of the subtidal bulge region. The dependence of $\Delta\rho_{\text{bulge}}/\Delta\rho_i$ on s_i and s_{bulge} is shown in Fig. 10b. Both s_i and s_{bulge} freshen with increasing discharge in rotational and nonrotational experiments, but the freshening effect of the added buoyancy is greater in
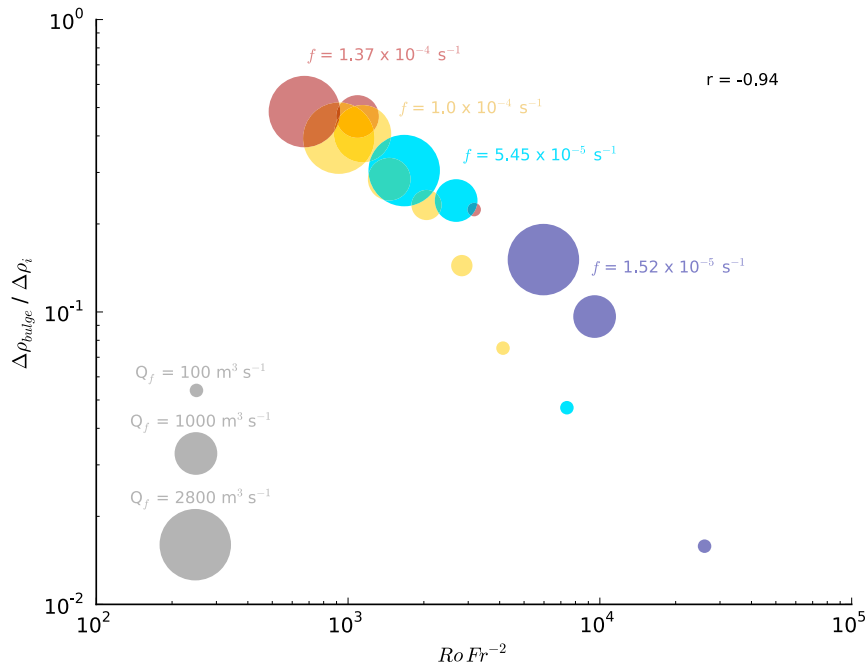
FIG. 8. Ratio of the far-field density anomaly $\Delta\rho_{\text{bulge}}$ to the density anomaly $\Delta\rho_i$ as a function of RoFr^{-2}, where Ro and Fr are inflow Rossby and Froude numbers for rotational plume experiments with different discharges at different latitudes. The size of the dots indicate discharge and colors indicate the Coriolis frequency.

the rotational case. Although the local shear mixing is stronger with higher discharge, it is not enough to fully mix the additional freshwater to near-ocean salinities before it enters the coastal current; this is reflected in the freshening of the isohaline freshwater volume curves with increasing discharge in Fig. 7.

Figure 5 shows that mixing rates are suppressed for two discharge rates depending on the inclusion of

rotation in the model. Although jet inertia pushes the edge of the bulge farther offshore in high discharge plumes, the added inflow buoyancy causes rotation to inhibit spreading in fresher isohalines relative to low discharge plumes. In nonrotational cases, the plume spreading is not inhibited by rotation; the transition to the far field happens farther offshore and the source water has undergone more mixing.
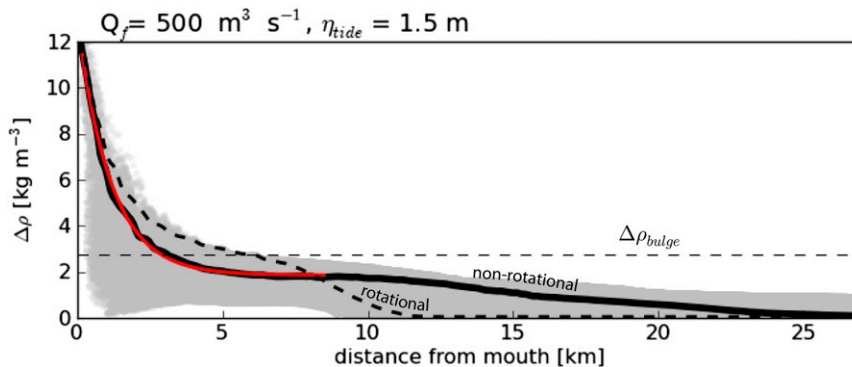

FIG. 9. Gray shaded region is domainwide upper-layer density anomaly over a tide for the $Q_f =$ 500 m^3 s^{-1} experiment without rotation. Solid black line is the tidal mean upper-layer density anomaly over an offshore transect from the mouth. The red line is the fit of an exponential decay function to the density anomaly for the inshore, concave portion of the transect. The thick black dashed line is the tidal mean upper-layer density anomaly along the offshore transect for the $Q_f =$ 500 m^3 s^{-1} experiment with $f = 10^{-4}$ s^{-1}. The thin, black, dashed line marks the density anomaly of water entering the coastal current for the $Q_f =$ 500 m^3 s^{-1} rotational experiment from Fig. 7.
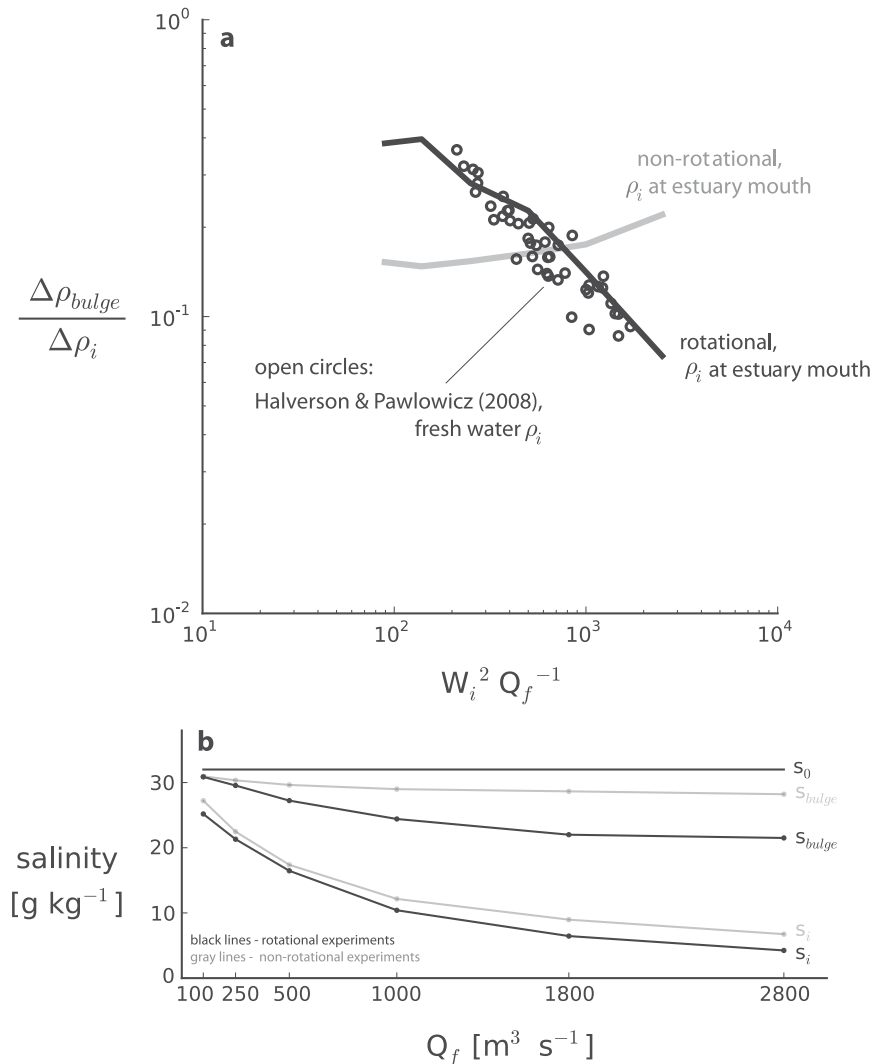
FIG. 10. (a) The ratio of the far-field density anomaly $\Delta\rho_{\text{bulge}}$ to the density anomaly $\Delta\rho_i$ (either at the estuary mouth or river mouth) as a function of $W_i^2 Q_f^{-1}$, where Q_f is freshwater discharge and W_i is estuary mouth width. Lines use ρ_i at the estuary mouth and open circles use freshwater ρ_i. The black line represents experiments with $f = 10^{-4}\,\text{s}^{-1}$, and the isopycnal where peak isohaline freshwater volume occurs (Fig. 7) is used for ρ_{bulge}. The gray line displays nonrotational experiments, and the offshore limit of the exponential fit to the density anomaly (Fig. 9) is used for $\Delta\rho_{\text{bulge}}$. Open circles are calculated from plume and reference salinity data from Halverson and Pawlowicz (2008). (b) The terms s_i, s_{bulge}, and s_0 in $f = 10^{-4}\,\text{s}^{-1}$ (black lines) and nonrotating (gray lines) cases.

Scaling arguments can be used to show that net mixing in the near field is sensitive to discharge. The supercritical Froude number criterion gives $\text{Fr}^2 = u^2/g'h \simeq 1$ at the lift off point. This relation, combined with the estuarine discharge $Q = uhW$, gives

$$U \sim \left(\frac{g'Q}{W}\right)^{1/3} \qquad (7)$$

as a scale for the inflow velocity. Figure 10 in Halverson and Pawlowicz (2008) indicates a roughly linear

relationship between plume surface area A_{plume} and river discharge, that is, $A_{\text{plume}} \sim c_A^{-1}Q$, where $c_A \sim 6.7 \times 10^{-6}\,\text{m}\,\text{s}^{-1}$. Therefore, $L \sim (c_A^{-1}Q)^{1/2}$, where L is the length scale associated with the inflow. As in this study, Hetland (2005) relates plume isohaline surface area to discharge rate and entrainment; therefore, the physical meaning of c_A is a mean vertical entrainment velocity over the entire area A [see Eq. (1); c_A is equivalent to w_e]. This estimate of entrainment velocity falls at the low end of the range of values shown in Fig. 3 in Hetland

(2010); it is small for near-field mixing. However, smaller values are expected for the mean vertical entrainment velocity since the very high mixing regions of the plume occur in a very small fraction of the total plume area. Similarly, Halverson and Pawlowicz (2011) calculate low values of entrainment in the Fraser plume because of spatial and temporal averaging.

A translational time scale related to advection L/U, which describes the time it takes for a particle to traverse the near-field plume, may be derived using the length and velocity scales of the plume given above:

$$T \sim \frac{Q^{1/6}W^{1/3}}{g'^{1/3}c_A^{1/2}}, \qquad (8)$$

implying that $T \propto Q^{1/6}W^{1/3}$.

Thus, as discharge increases, the quantity of water released lengthens the near field faster than it speeds up the flow, increasing the time scale [U scales as $Q^{1/3}$ in Eq. (7) and L scales as $Q^{1/2}$]. Furthermore, as the mouth width increases, the outflow is less constricted, leading to a weaker jet and a longer time scale; mouths that are much wider than the deformation radius are not constricting and likely do not produce a near-field plume. Applying $5000\,\mathrm{m}^3\,\mathrm{s}^{-1}$ for Q, 1 km for W, and $0.25\,\mathrm{m\,s}^{-2}$ for g' gives the translational time scale for the Fraser inflow as $T \sim 7$ h; normalizing by the rotational period gives $Tf \sim 2.5$, indicating that the translational time scale exceeds the rotational time scale and rotation strongly limits near-field spreading.

The density anomaly ratio is correlated with Tf: the larger Tf, the larger the ratio (i.e., less net mixing in the plume). If rotation is included in the solution, it will always limit net mixing, and Tf reveals how much. Only in the simulations where rotation is completely removed does net mixing increase with discharge and all plumes become mixed to the far-field asymptotic salinity.

Hetland and MacDonald (2008) show that, within the core of the near field, plume parameters, including shear mixing, are a function of radial distance from the mouth, and the effect of rotation is to deflect streamlines to the right (in the Northern Hemisphere). The effect of curved streamlines in the core of the near field by rotation is evidenced in Figs. 7 and 8, indicating that rotation plays a role in limiting mixing throughout the plume interior. Where freshwater volume in an isohaline is low, strong mixing has diluted plume water to higher salinities; Fig. 7 shows that mixing is stronger in the $Q_f = 1000\,\mathrm{m}^3\,\mathrm{s}^{-1}$ nonrotational simulation than in the rotational simulation at nearly all plume salinity classes, including fresh isohalines near the mouth. The rotational arrest of the near field occurs over many kilometers; the prominent trend in $\Delta\rho_{\mathrm{bulge}}/\Delta\rho_i$ in Fig. 8

suggests that even low discharge, low-latitude plumes, where the scale of the near field is less than the deformation radius, experience the effect of rotation-suppressing mixing in the near field. To what extent net mixing in nonrotational plumes is larger because the local mixing is stronger or because the spatial scales over which mixing takes place are larger is not evaluated in this work. The scaling here focuses on the observed relationship between discharge and plume area.

Another significant result of the experiments is the relationship between RoFr^{-2} and net mixing in rotational plumes. Garvine (1999) shows the same functional dependence in plume behavior and calls the inverse of RoFr^{-2} the "scaled inlet transport number." The inlet transport number is the fundamental dimensionless parameter that governs the flow, and, along with the mouth Kelvin and Reynolds numbers, tidal amplitude and bottom slope completely describes the downshelf penetration and cross-shelf extent of the plume. The values of the inlet transport number in the idealized cases fall at the small, surface-advected plume end of the Garvine (1999) parameter space, where there is more scatter in the functional relationship. This could explain why net mixing trends in rotational and irrotational experiments are not captured in Fig. 8 as f approaches zero.

The relationship between the inlet transport number, the scales of plume penetration, and net plume mixing suggested by these studies are consistent with the idea that rotation inhibits the near field, limiting the shear mixing plume area and reducing net mixing. Furthermore, Garvine (1999) notes that penetration values are sensitive to mixing parameters in his simulations; to observe the same relationship in field measurements is further proof that the inlet transport number is salient.

The results of this analysis are sensitive to the scaling relationships illustrated in Halverson and Pawlowicz (2008) that are convincing but somewhat uncertain because of temporal and spatial limitations in ferry sampling. For example, their study indicates that c_A, or the mean vertical entrainment velocity w_e in their manuscript, decreases with increasing river discharge. This relationship implies that Q and plume area A may not be exactly linearly related, but the relationship is still likely captured by a positive power dependence (this is reasonable since in observed plumes g' also increases with discharge, affecting A). Since w_e in Halverson and Pawlowicz (2008) is an average entrainment over the plume base, it is plausible that this quantity would decrease as A increases at a faster rate than Q. To show that our conclusions still hold, working the relationship $w_e \sim Q^{-1}$ into the above equations gives an even tighter relationship between Q and the translational time scale T.

Although the Fraser River plume observations likely include mixing through the near field and midfield (or bulge region) at times, they are comparable to the net mixing estimates from our model experiments because both target asymptotic values outside the core of the near field. We are comparing tendencies in parameter space in our analysis of rotational and nonrotational model experiments and field measurements, so it should not matter what definition of water feeding the far field we use, all of the definitions scale similarly in parameter space. It is reasonable to compare net mixing trends in Fig. 10a, however, values of net mixing should be quantitatively compared with caution between experiments where different methods are used to evaluate $\Delta\rho_{\text{bulge}}$.

The tidal pulsing and ambient flow in these experiments support a different physical environment than the steady, pure radial spreading plume experiments described in Hetland (2010). The addition of realistic physical forcing allows comparison with field data as rotation, tides, and ambient currents are important elements to the Fraser plume evolution. Halverson and Pawlowicz (2008) suggest that wind-driven circulation in the semienclosed Strait of Georgia may differ from the wind-driven circulation on the shelf, so we exclude wind forcing from our experiments. The experiments in this paper explain the results of Hetland (2010) and Halverson and Pawlowicz (2008), focusing only on shear mixing through the near/midfield region.

7. Conclusions

This study demonstrates the importance of rotation in determining the evolution of the near-field plume. The primary finding of this study is that rotation is effective in limiting net plume mixing. The arrest of the interfacial shear-mixing region by rotation results in water leaving the near-field plume that is not as modified as an advective measure, such as the jet-to-plume length scale, would predict.

Besides showing the impact of rotation on net mixing, these experiments illustrate net mixing trends in plumes with time-dependent estuarine discharge. The results of this study are especially relevant to plumes with highly variable discharge, such as the Eel River plume in northern California, that exhibit source flux variability across several orders of magnitude.

The combined effect of rotation and increasing discharge leads to less net mixing, while the effect of increasing discharge and the absence of rotation leads to greater net mixing. Increasing transport at the river mouth strengthens mixing near the source, and increasing buoyancy input enhances the spreading and shear mixing in the plume, ergo an increasingly mixed

far-field plume with increasing discharge in a nonrotational environment. However, rotation redirects the flow downcoast, curbing shear mixing while preventing further radial spreading, resulting in a more stratified far-field plume when discharge is increased.

To provide a realistic representation of early plume evolution, rotation is a critical element to include in a near-field model; the rotational parameter will alter near-field density structure and therefore when and where a plume transitions to subcritical. The far-field density anomaly provides the boundary condition for the coastal current and offshore shelf circulation, so understanding how much mixing happens in the near- and midfield provides a link between plume studies focused on these regions.

REFERENCES

Canuto, V. M., A. Howard, Y. Cheng, and M. S. Dubovikov, 2001: Ocean turbulence. Part I: One-point closure model—Momentum and heat vertical diffusivities. *J. Phys. Oceanogr.*, **31**, 1413–1426, doi:10.1175/1520-0485(2001)031<1413:OTPIOP>2.0.CO;2.

Chapman, D. C., 1985: Numerical treatment of cross-shelf open boundaries in a barotropic coastal ocean model. *J. Phys. Oceanogr.*, **15**, 1060–1075, doi:10.1175/1520-0485(1985)015<1060:NTOCSO>2.0.CO;2.

Chen, F., and D. G. MacDonald, 2006: Role of mixing in the structure and evolution of a buoyant discharge plume. *J. Geophys. Res.*, **111**, C11002, doi:10.1029/2006JC003563.

——, ——, and R. D. Hetland, 2009: Lateral spreading of a near-field river plume: Observations and numerical simulations. *J. Geophys. Res.*, **114**, C07013, doi:10.1029/2008JC004893.

Flather, R. A., 1976: A tidal model of the northwest European continental shelf. *Mem. Soc. Roy. Sci. Liege*, **10** (6), 141–164.

Fong, D. A., and W. R. Geyer, 2001: Response of a river plume during an upwelling favorable wind event. *J. Geophys. Res.*, **106**, 1067–1084, doi:10.1029/2000JC900134.

Garvine, R. W., 1982: A steady state model for buoyant surface plume hydrodynamics in coastal waters. *Tellus*, **34**, 293–306, doi:10.1111/j.2153-3490.1982.tb01818.x.

——, 1984: Radial spreading of buoyant, surface plumes in coastal waters. *J. Geophys. Res.*, **89**, 1989–1996, doi:10.1029/JC089iC02p01989.

——, 1987: Estuary plumes and fronts in shelf waters: A layer model. *J. Phys. Oceanogr.*, **17**, 1877–1896, doi:10.1175/1520-0485(1987)017<1877:EPAFIS>2.0.CO;2.

——, 1999: Penetration of buoyant coastal discharge onto the continental shelf: A numerical model experiment. *J. Phys. Oceanogr.*, **29**, 1892–1909, doi:10.1175/1520-0485(1999)029<1892:POBCDO>2.0.CO;2.

Halverson, M. J., and R. Pawlowicz, 2008: Estuarine forcing of a river plume by river flow and tides. *J. Geophys. Res.*, **113**, C09033, doi:10.1029/2008JC004844.

——, and ——, 2011: Entrainment and flushing time in the Fraser River estuary and plume from a steady salt balance analysis. *J. Geophys. Res.*, **116**, C08023, doi:10.1029/2010JC006793.

Hetland, R. D., 2005: Relating river plume structure to vertical mixing. *J. Phys. Oceanogr.*, **35**, 1667–1688, doi:10.1175/JPO2774.1.

——, 2010: The effects of mixing and spreading on density in near-field river plumes. *Dyn. Atmos. Oceans*, **49**, 37–53, doi:10.1016/j.dynatmoce.2008.11.003.

——, and D. G. MacDonald, 2008: Spreading in the near-field Merrimack River plume. *Ocean Modell.*, **21**, 12–21, doi:10.1016/j.ocemod.2007.11.001.

Jirka, G. H., 2007: Buoyant surface discharges into water bodies. II: Jet integral model. *J. Hydrol. Eng.*, **133**, 1021–1036, doi:10.1061/(ASCE)0733-9429(2007)133:9(1021).

Jones, G. R., J. D. Nash, R. L. Doneker, and G. H. Jirka, 2007: Buoyant surface discharges into water bodies. I: Flow classification and prediction method. *J. Hydrol. Eng.*, **133**, 1010–1020, doi:10.1061/(ASCE)0733-9429(2007)133:9(1010).

Jurisa, J. T., and R. J. Chant, 2013: Impact of offshore winds on a buoyant river plume system. *J. Phys. Oceanogr.*, **43**, 2571–2587, doi:10.1175/JPO-D-12-0118.1.

Kakoulaki, G., 2015: Using Lagrangian surface drifters to study wind forcing and lateral spreading in a buoyant river plume. Ph.D. thesis, University of Massachusetts Dartmouth, 116 pp.

Kostaschuk, R., and L. Atwood, 1990: River discharge and tidal controls on salt-wedge position and implications for channel shoaling: Fraser River, British Columbia. *Can. J. Civ. Eng.*, **17**, 452–459, doi:10.1139/l90-049.

Lentz, S. J., and K. R. Helfrich, 2002: Buoyant gravity currents along a sloping bottom in a rotating fluid. *J. Fluid Mech.*, **464**, 251–278, doi:10.1017/S0022112002008868.

MacCready, P., R. D. Hetland, and W. R. Geyer, 2002: Long-term isohaline salt balance in an estuary. *Cont. Shelf Res.*, **22**, 1591–1601, doi:10.1016/S0278-4343(02)00023-7.

MacDonald, D. G., and W. R. Geyer, 2004: Turbulent energy production and entrainment at a highly stratified estuarine front. *J. Geophys. Res.*, **109**, C05004, doi:10.1029/2003JC002094.

——, and ——, 2005: Hydraulic control of a highly stratified estuarine front. *J. Phys. Oceanogr.*, **35**, 374–387, doi:10.1175/JPO-2692.1.

——, L. Goodman, and R. D. Hetland, 2007: Turbulent dissipation in a near-field river plume: A comparison of control volume and microstructure observations with a numerical model. *J. Geophys. Res.*, **112**, C07026, doi:10.1029/2006JC004075.

Marchesiello, P., J. C. McWilliams, and A. Shchepetkin, 2001: Open boundary condition for long-term integration of regional oceanic models. *Ocean Modell.*, **3**, 1–20, doi:10.1016/S1463-5003(00)00013-5.

McCabe, R. M., B. M. Hickey, and P. MacCready, 2008: Observational estimates of entrainment and vertical salt flux in the interior of a spreading river plume. *J. Geophys. Res.*, **113**, C08027, doi:10.1029/2007JC004361.

——, P. MacCready, and B. M. Hickey, 2009: Ebb-tide dynamics and spreading of a large river plume. *J. Phys. Oceanogr.*, **39**, 2839–2856, doi:10.1175/2009JPO4061.1.

O'Donnell, J., 1990: The formation and fate of a river plume: A numerical model. *J. Phys. Oceanogr.*, **20**, 551–569, doi:10.1175/1520-0485(1990)020<0551:TFAFOA>2.0.CO;2.

Shchepetkin, A. F., and J. C. McWilliams, 2005: The Regional Oceanic Modeling System (ROMS): A split-explicit, free-surface, topography-following-coordinate oceanic model. *Ocean Modell.*, **9**, 347–404, doi:10.1016/j.ocemod.2004.08.002.

Smolarkiewicz, P. K., and T. L. Clark, 1986: The multidimensional positive definite advection transport algorithm: Further development and applications. *J. Comput. Phys.*, **67**, 396–438, doi:10.1016/0021-9991(86)90270-6.

Umlauf, L., L. Arneborg, H. Burchard, V. Fiekas, H. U. Lass, V. Mohrholz, and H. Prandke, 2007: Transverse structure of turbulence in a rotating gravity current. *Geophys. Res. Lett.*, **34**, L08601, doi:10.1029/2007GL029521.

Yankovsky, A. E., and D. C. Chapman, 1997: A simple theory for the fate of buoyant coastal discharges. *J. Phys. Oceanogr.*, **27**, 1386–1401, doi:10.1175/1520-0485(1997)027<1386:ASTFTF>2.0.CO;2.

——, B. M. Hickey, and A. K. Münchow, 2001: Impact of variable inflow on the dynamics of a coastal buoyant plume. *J. Geophys. Res.*, **106**, 19 809–19 824, doi:10.1029/2001JC000792.